Remote Sensing of Environment 331 (2025) 115057

Contents lists available at ScienceDirect

Remote Sensing of Environment

journal homepage: www.elsevier.com/locate/rse

Volcanic sulfur dioxide monitored from a constellation of FengYun hyperspectral infrared sounders in dawn-dusk, mid-morning, and afternoon sun-synchronous orbits

Zhao-Cheng Zeng [a,*], Lieven Clarisse [b], Bruno Franco [b], Cathy Clerbaux [c,b], Nicolas Theys [d], Chengli Qi [e], Lu Lee [e], Lin Zhu [e], Xiuqing Hu [e], Mingjian Gu [f], Peng Zhang [g]

[a] School of Earth and Space Sciences, Peking University, Beijing, China
[b] Spectroscopy, Quantum Chemistry and Atmospheric Remote Sensing (SQUARES), Brussels Laboratory of the Universe (BLU-ULB), Université Libre de Bruxelles (ULB), Brussels, Belgium
[c] LATMOS/IPSL, Sorbonne Université, UVSQ, CNRS, Paris, France
[d] Royal Belgian Institute for Space Aeronomy (BIRA-IASB), Brussels, Belgium
[e] National Satellite Meteorological Center, China Meteorological Administration, Beijing, China
[f] Shanghai Institute of Technical Physics, Chinese Academy of Sciences, Shanghai, China
[g] Meteorological Observation Center of China Meteorological Administration, Beijing, China

ARTICLE INFO

Edited by Menghua Wang

Keywords:
Volcanic sulfur dioxide
Satellite constellation
FengYun hyperspectral infrared sounders
Sun-synchronous orbits
Dawn-dusk orbit

ABSTRACT

Satellite observations offer a unique way of monitoring the spatial distribution, vertical structure and temporal variation of volcanic sulfur dioxide (SO_2) plumes. In this study, we use observations from the Hyperspectral Infrared Atmospheric Sounder (HIRAS) constellation on board China's FengYun-3 (FY-3) meteorological satellites flying in three different sun-synchronous orbits, including dawn-dusk, mid-morning, and afternoon orbits. The constellation provides six global coverages (roughly every 4-h) each day, with equatorial overpass times at 5:30 am/pm for FY-3E, 10:00 am/pm for FY-3F, and 2:00 am/pm for FY-3D. We retrieve SO_2 total column and layer height from the Ruang volcanic eruptions in April 2024. The retrievals show consistency among the different HIRAS and are highly correlated with IASI and TROPOMI observations. The e-folding time of the volcanic SO_2 mass is estimated to be 9.0 ± 2.8 days, which is representative of a plume in the Upper Troposphere-Lower Stratosphere (UTLS). Lastly, we apply the methods to the eruptions of the Russia's Sheveluch volcano in November 2024 at high latitudes and show the effectiveness and high consistency among the HIRAS sensors in detecting the SO_2 signal. This study demonstrates the capability of a global constellation of FengYun hyperspectral infrared sounders to monitor SO_2 emissions from volcanic eruptions.

1. Introduction

Sulfur emissions from volcanic eruptions account for 7.5–10.5 % of global sulfur emissions annually (Halmer et al., 2002). Sulfur dioxide (SO_2) injected into the Upper Troposphere-Lower Stratosphere (UTLS) from volcanic eruptions can have significant impacts on atmospheric chemistry and climate (Robock, 2000). The sulfuric acid aerosols from the oxidation of SO_2 in the stratosphere can efficiently reflect solar radiation and affect the Earth's energy balance for years (Robock, 2000). Tracking volcanic SO_2 plumes provides important information for the study of the co-emitted volcanic ash (Prata and Kerkmann, 2007; Sellitto et al., 2024) and for understanding the climate impacts of volcanic emissions (e.g., Robock, 2000). In addition, it is also important for monitoring volcanic activity (Pardini et al., 2019) and for mitigating aviation hazards associated with volcanic sulfuric acid clouds that can reduce visibility and damage aircraft engines (e.g., Prata, 2009).

Satellite observations offer a unique way of tracking the spatial distribution, vertical structure, and temporal variation of volcanic SO_2 plumes. Nadir viewing satellites observing in the ultraviolet spectral region include, among others, TOMS, GOME/GOME-2, SCIAMACHY, OMI, and TROPOMI (e.g., Krueger et al., 1995; Rix et al., 2012; Lee et al., 2008; Carn et al., 2008; Queißer et al., 2019; Theys et al., 2021). In the infrared, these satellites include MODIS, AVHRR, TOVS, and ASTER (e.g., Watson et al., 2004; Prata, 1989; Prata et al., 2003; Pugnaghi et al.,

* Corresponding author.
E-mail address: zczeng@pku.edu.cn (Z.-C. Zeng).

https://doi.org/10.1016/j.rse.2025.115057
Received 31 July 2025; Received in revised form 14 September 2025; Accepted 29 September 2025
Available online 4 October 2025

2006), Hyperspectral infrared IR sounders: AIRS, TES, IASI, and CrIS (e.g., Carn et al., 2005; Clerbaux et al., 2008; Clarisse et al., 2008; Walker et al., 2011; Carboni et al., 2012; Hyman and Pavolonis, 2020). In addition, the Microwave Limb Sounder (e.g., Pumphrey et al., 2015), a limb sounder, and the Atmospheric Chemistry Experiment – Fourier Transform Spectrometer (e.g., Dodangodage et al., 2025), a solar occultation instrument, also measure SO_2 from volcanic eruptions. All of the above instruments show high sensitivity to large SO_2 enhancements from volcanic plumes. However, most of these studies focus on the detection of volcanic SO_2 emissions from a single orbit. Here we explore the potential of a constellation of three hyperspectral infrared sounders in three different low Earth orbits to track SO_2 plumes globally with high temporal frequency.

The Hyperspectral Infrared Atmospheric Sounder (HIRAS) instruments on board China's FengYun-3 (FY-3) meteorological satellites fly in three different sun-synchronous orbits, including dawn-dusk, mid-morning, and afternoon orbits, forming a low-Earth orbit constellation (see Fig. 1). The constellation provides six global coverages (roughly every 4-h) each day. As shown in Fig. 1(a), their equatorial overpass times are 5:30 am/pm for FY-3E, 10:00 am/pm for FY-3F, and 2:00 am/pm for FY-3D. While sensors such as IASI use the mid-morning orbit and sensors such as TROPOMI and CrIS use the early afternoon orbit, the observational benefits of dawn-dusk orbit, in which FY-3E is currently flying (Zhang et al., 2024), has received far less investigation. The HIRAS sensors on board the FY-3 series have demonstrated their capability to detect atmospheric compounds (e.g., Xie et al., 2023), including carbon monoxide (CO; Zeng, 2025), ammonia (Zhou et al., 2024), and volatile organic compounds (VOC; Hua et al., 2025; Liang et al., 2025). Recently, Li et al. (2025) conducted a series of channel selection experiments to detect volcanic SO_2 using FY-3E/HIRAS-II spectra based on brightness temperature differences. However, this study does not include quantitative retrievals of SO_2 columns from the HIRAS spectra. The capability of HIRAS observations to monitor the variability of volcanic SO_2 columns, particularly with regard to quantifying SO_2 layer height, has not yet been evaluated.

This study aims to demonstrate, for the first time, the capability of a global constellation of FengYun hyperspectral infrared sounders to monitor volcanic SO_2 plumes with a high observation frequency of 4-h each day. We use infrared spectra (1208.75 to 1400 cm^{-1}) from a constellation of HIRAS on board FY-3D, FY3E, and FY-3F to track SO_2 from the mid-April 2024 Ruang volcanic eruption. Intercomparisons of the SO_2 total column and SO_2 layer height with IASI and TROPOMI are performed. Observations from April 17 to 29, 2024 are used to estimate the lifetime of the atmospheric SO_2 plume. In addition, we apply the methods to the eruptions of the Russia's Sheveluch volcano in November 2024 to investigate the effectiveness and consistency of the HIRAS sensors in detecting the SO_2 signal at high latitudes. Such a Low-Earth-Orbit (LEO) satellite constellation is both unique and novel from the perspective of Earth observation. The HIRAS SO_2 data, as demonstrated in this study, can serve as a valuable addition to the current capabilities for global volcanic SO_2 monitoring.

The structure of this paper is as follows: Section 2 introduces the HIRAS instrument. The retrieval algorithms for SO_2 column and layer height are described in Section 3. Section 4 provides the retrieval results and cross-comparisons with IASI and TROPOMI. Discussion and the conclusions are in Section 5.

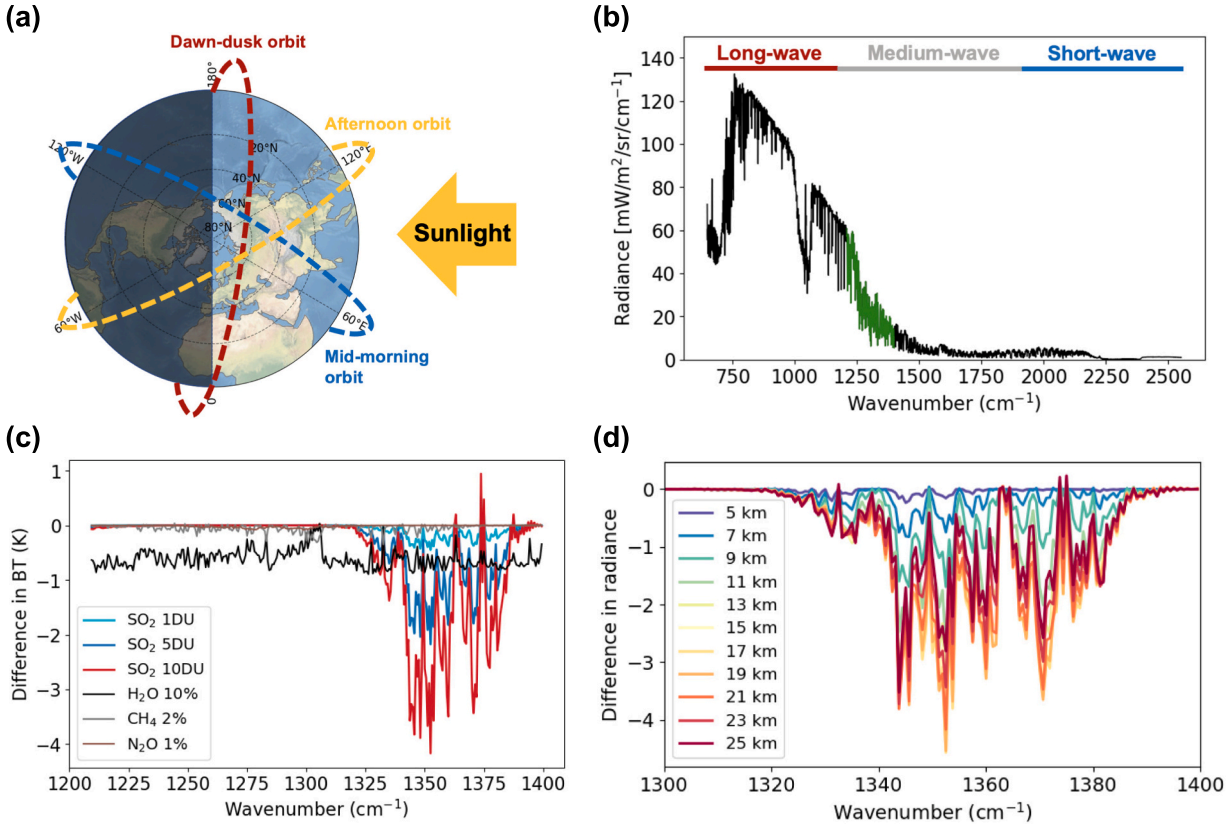

Fig. 1. (a) The constellation of HIRAS on board the FengYun-3 satellite series in dawn-dusk, mid-morning, and afternoon sun-synchronous orbits; (b) Sample spectra from FY-3E/HIRAS-II, including short-wave, mid-wave, and long-wave wavelengths. The spectral range in green (1208.75 to 1400 cm^{-1}) is used in this study, which includes the SO_2 $\nu 3$ absorption over 1300–1400 cm^{-1}. (c) The SO_2 absorption feature for a SO_2 layer at 10 km (with a thickness of 1 km) with a partial column of 1, 5 and 10 DU. The main interference from H_2O (10 % change) is also shown, as well as CH_4 (2 % change) and N_2O (1 % change); (d) An illustration of the constructed Jacobian for SO_2 at different altitudes from 5 km to 25 km for every 2 km. The Jacobian is generated with a forward radiative transfer model (see Section 3). (For interpretation of the references to colour in this figure legend, the reader is referred to the web version of this article.)

2. Hyperspectral InfraRed atmospheric sounder (HIRAS)

The HIRAS on board the FY-3 satellite series is a Fourier Transform Michelson interferometer that collects upwelling infrared radiation in three spectral windows, i.e., the short-wave, mid-wave, and long-wave spectral bands (Fig. 1b). A summary of the instrumental characteristics for HIRAS on board FY-3D, FY-3E, and FY-3F is provided in Table I. The 1st generation of HIRAS on board FY-3D, hereafter referred to as FY-3D/HIRAS, was launched in 2017 (Wu et al., 2020). The 2nd generation of HIRAS on board FY-3E and FY-3F was launched in 2021 and 2023, respectively (Zhang P. et al., 2022, Zhang C. et al. 2022). Similar to IASI and CrIS, this study uses the SO_2 $\nu 3$ absorption band, which is the strongest in the mid-infrared, to retrieve SO_2 column and layer height. The spectral noise in this spectral region for the three HIRAS instruments is shown in Fig. S1. In the SO_2 $\nu 3$ absorption region at 1300–1400 cm^{-1}, the averaged noise equivalent differential temperature (NEdT) of FY-3D/HIRAS is about 0.10 K at 280 K blackbody, better than 0.10 K for FY-3E/HIRAS-II, and about 0.05 K for FY-3F/HIRAS-II, indicating a potentially high sensitivity to SO_2 from volcanic eruptions. The noise level over this spectral range is slightly larger than IASI (0.05 K; Clarisse et al., 2008) and CrIS (lower than 0.05 K; Hyman and Pavolonis, 2020). As shown in Table 1, FY-3D/HIRAS has slightly coarser resolution (16 km) at nadir compared to FY-3E/HIRAS-II (14 km) and FY-3F/HIRAS-II (14 km). The spectral window covering the strong SO_2 $\nu 3$ absorption (Fig. 1b) is used for the SO_2 retrieval in this study, similar to the methods developed by Carboni et al. (2012) and the SO_2 height estimation method by Clarisse et al. (2014). The main interfering gases are water vapor (H_2O), nitrous oxide (N_2O), and methane (CH_4). Assuming a volcanic SO_2 layer located at 10 km, the absorption features of SO_2 are distinct from those of the interfering gases, as shown in Fig. 1(c).

3. Retrieval methods of SO_2 column and layer height from HIRAS spectra

The workflow of the retrieval algorithms to estimate SO_2 columns and layer heights from the HIRAS instruments on board FY-3D, FY-3E, and FY-3F is outlined in Fig. 2. Details on the radiative transfer model, the detection of volcanic SO_2 (step 1), and the estimation of SO_2 layer height (step 2) and column (step 3) are provided below.

3.1. Radiative transfer model in FY-LeoAIR

The FengYun Low Earth Orbit Atmospheric Infrared Retrieval (FY-LeoAIR) is adapted from the algorithm developed for the retrieval of CO, NH_3, and HCOOH (Zeng et al., 2023a; Zeng et al., 2023b; Zeng et al., 2024) from the Geostationary Interferometric Infrared Sounder (GIIRS) observations. FY-LeoAIR has been successfully applied to retrieve CO and VOCs (e.g., Zeng, 2025; Hua et al., 2025) from FY-3E/HIRAS-II. The radiative transfer model in FY-LeoAIR simulates the upwelling infrared radiance by summing up four components: the upward surface infrared radiation, the upward atmospheric infrared radiation, the surface-reflected component of the downward atmospheric infrared radiation, and the incoming solar radiation reflected by the surface (Zeng et al., 2023a). The atmosphere in the forward radiative transfer model is separated into 34 layers, spaced at 1 km intervals from the surface up to 1 hPa. In the infrared spectral region for SO_2 retrieval (1300 cm^{-1} to 1400 cm^{-1}), molecular and aerosol scattering is very small and is therefore not considered. For the molecular absorption coefficients (ABSCO), we use the Line-By-Line Radiative Transfer Model (LBLRTM v12.11; Atmospheric and Environmental Research, 2025) to construct look-up tables under different temperatures and atmospheric pressures. The a priori surface and atmospheric parameters in the radiative transfer model are listed in Table 2. The a priori surface and atmospheric variables are extracted from the European Centre for Medium-Range Weather Forecasts (ECMWF) Reanalysis v5 (ERA5) (Hersbach et al., 2020). Surface variables include surface pressure and surface skin temperature, while atmospheric variables comprise atmospheric temperature, water vapor, and ozone. For interfering gases, CO_2 is extracted from the ECMWF-CAMS model, and a priori profiles for other interfering gases are taken from the LBLRTM standard atmosphere. The background SO_2 (as shown in Fig. S2) represents the background conditions without volcanic contribution. The surface emissivity is extracted from the Global Infrared Land Surface Emissivity: UW-Madison Baseline Fit Emissivity Database (Seemann et al., 2008). The ocean emissivity model in Masuda et al. (1998) is adopted to calculate the ocean surface emissivity. A full description of the forward radiative transfer model is provided in Zeng et al. (2023a).

The Jacobian vectors of the SO_2 absorption are calculated using the forward radiative transfer model and then used in Section 3.2 and 3.3 to retrieve the SO_2 layer height. The Jacobian is derived by finite difference using a total SO_2 column of 1 DU, which is about 10 times the a priori. In Section 3.3, the Jacobian vectors at different altitudes (shown in Fig. 1 (d)) are calculated by assigning the SO_2 partial column (10 DU) to different layers at different heights.

3.2. Detection of SO_2 plume

In this study, the Hyperspectral Range Index (HRI) is calculated for the detection of SO_2. The HRI has been shown to be effective for detecting infrared absorbers such as SO_2 (e.g., Walker et al., 2011; Clarisse et al., 2014). It quantifies the magnitude of SO_2 absorption through a weighted integration of contributions from all spectral channels. The HRI is defined as:

$$\mathbf{HRI} = \frac{\boldsymbol{K}^T\boldsymbol{S}^{-1}(\boldsymbol{y}-\bar{\boldsymbol{y}})}{\sqrt{\boldsymbol{K}^T\boldsymbol{S}^{-1}\boldsymbol{K}}} \quad (1)$$

where $\mathbf{K}$ is the Jacobian, defined as the change in radiance relative to the change in SO_2 column. $\bar{\boldsymbol{y}}$ and $\mathbf{S}$ are the mean spectrum and its associated covariance matrix, respectively calculated from a set of background spectra. They represent the mean state and variation to be expected from the spectral observations in the absence of SO_2. In this study, spectral observations on April 16 over a clean region (−20°W to 140°E, −15°S to 15°N) are used to construct the background spectral mean and the

Table 1
Summary of the instrumental characteristics for HIRAS on board FY-3D, FY-3E, and FY-3F.

Instruments	Spectra range (cm^{-1})	Spatial resolution (km)	Spectral resolution (cm^{-1})	Characteristics	Refs
FY-3D/ HIRAS	LW: 648.75–1136.25 MW: 1208.75–1751.25 SW: 2153.75–2551.25	16	0.625	FOR: 2 × 2 FOVs FOV: 1.1° ECT: 2 am/pm	Qi et al. (2020)
FY-3E/ HIRAS-II	LW: 648.75–1169.375 MW: 1167.5–1921.25 SW: 1919.375–2551.25	14	0.625	FOR: 3 × 3 FOVs FOV: 1.0° ECT: 5:30 am/pm	Zhang et al. (2022a, 2022b)
FY-3F/ HIRAS-II	LW: 648.75–1169.375 MW: 1167.5–1921.25 SW: 1919.375–2551.25	14	0.625	FOR: 3 × 3 FOVs FOV: 1.0° ECT: 10 am/pm	Zhang et al. (2022a, 2022b)

Notes: FOR (field-of-regard); FOV (field of views); ECT (Equatorial crossing time); LW (Long-wave); MW (medium-wave); SW (short-wave).

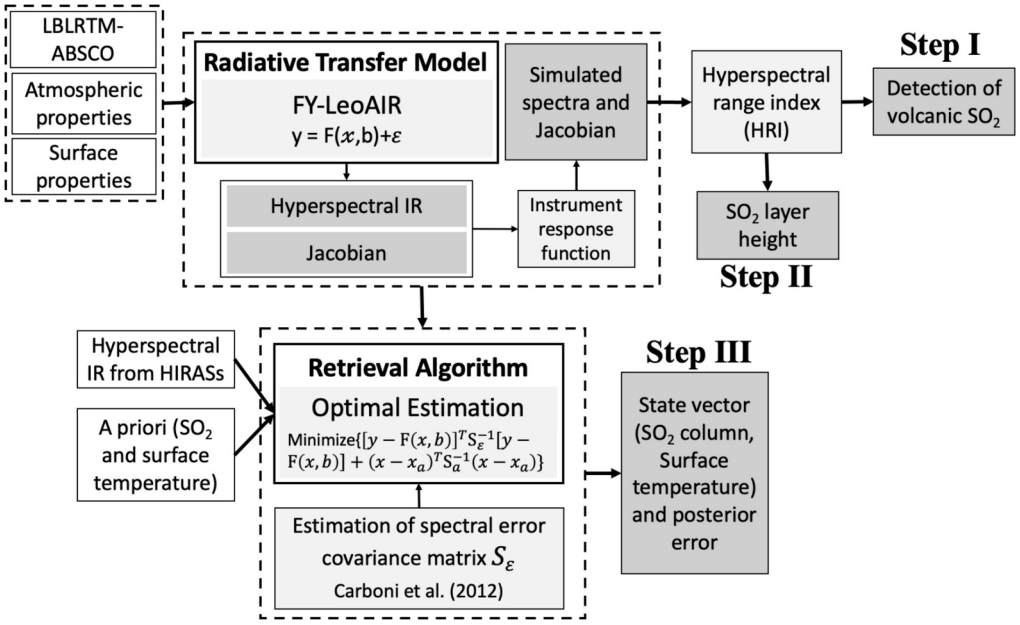

Fig. 2. Framework of methodology to estimate SO_2 columns and layer heights from HIRAS on board FY-3D, FY-3E, and FY-3F. Details of steps I, II, and III are provided in Sections 3.2, 3.3, and 3.4, respectively.

Table 2
Surface and atmospheric parameters in the radiative transfer model of FY-LeoAIR.

Variable types	Variables	Sources	References
Atmospheric properties	SO_2	LBLRTM	Atmospheric and Environmental Research (2025)
	H_2O, O_3	ECMWF-ERA5	Hersbach et al. (2020)
	CO_2	ECMWF-CAMS	Inness et al. (2019)
	Interfering gases: HNO_3, CH_4, N_2O	LBLRTM	Atmospheric and Environmental Research (2025)
	Atmospheric temperature	ECMWF-ERA5	Hersbach et al. (2020)
Surface properties	Land emissivity	UW-Madison Emissivity Database	Seemann et al. (2008)
	Ocean emissivity	Ocean emissivity model	Masuda et al. (1998)
	Pressure	ECMWF-ERA5	Hersbach et al. (2020)
	Temperature	ECMWF-ERA5	Hersbach et al. (2020)

covariance matrix. Spectral data from all three HIRAS instruments are combined to calculate the matrix to ensure consistency of the detection results. Unfortunately, in humid atmosphere like the tropics, due to the strong H_2O absorption in the SO_2 $\nu 3$ absorption window, infrared observations are sensitive to SO_2 only in the higher troposphere (Clarisse et al., 2014). For strong volcanic eruptions, which typically inject an SO_2 plume into the atmosphere above 10 km, infrared observations have shown high sensitivity (e.g., Walker et al., 2011; Clarisse et al., 2014). Note that HIRAS also covers the SO_2 $\nu 1$ band, which exhibits weaker absorption. Additionally, the magnitude of the HRI is not linearly proportional to the SO_2 column, as the correlation is affected by thermal contrast (TC) and the altitude of SO_2. TC is defined as the difference in temperatures of the surface and the SO_2 layer.

3.3. Retrieval of SO_2 layer height

The retrieval algorithm for estimating the SO_2 layer height is based on the HRI in eq. (1). The idea behind this algorithm is to exploit the fact that the SO_2 spectral signature (i.e., its Jacobian) varies significantly with the altitude of the SO_2 layer due to strong interferences with H_2O absorption features (Clarisse et al., 2014). The first step in the algorithm is to generate Jacobian vectors using the FY-LeoAIR algorithm (Zeng, 2025) with SO_2 layer located at different altitudes. The second step involves calculating HRI values at different altitudes, denoted as HRI(h), using the corresponding Jacobian at each altitude. Theoretically, if the actual SO_2 layer is located at height h*, then HRI(h*) should have the largest value. The distinctive absorption features at different altitudes allow the retrieval of SO_2 layer height.

The absolute values of the SO_2 Jacobian at different heights, used to calculate the HRI, are affected not only by the SO_2 layer height but also by the H_2O profile, as well as surface and atmospheric properties. However, the relative difference in the SO_2 Jacobian at different heights is more important in the derivation of SO_2 layer height, because the layer height is retrieved as the altitude at which HRI(h) reaches its maximum value. In addition, the variability of H_2O abundance at high altitudes around UTLS is relatively small compared to lower atmosphere, and therefore, its contribution to the SO_2 layer height estimation uncertainty is limited. Consequently, this relative difference in the SO_2 Jacobian is primarily driven by the change of SO_2 layer height, and the effectiveness of this method has been demonstrated in Clarisse et al. (2014) in validation with MLS and CALIPSO observations. In addition, the clouds below the SO_2 plume do not affect the retrieval of SO_2 layer height using this method.

3.4. Retrieval of SO_2 total column

The FY-LeoAIR retrieval algorithm (Zeng, 2025; Zeng et al., 2024) based on optimal estimation method (Rodgers, 2000) is adapted to estimate the SO_2 total column following Carboni et al. (2012). The retrieval algorithm aims to minimize the following cost function:

$$\boldsymbol{J}(\boldsymbol{x}) = [\boldsymbol{y} - \mathbf{F}(\boldsymbol{x}, \boldsymbol{b})]^T \mathbf{S}_\epsilon^{-1} [\boldsymbol{y} - \mathbf{F}(\boldsymbol{x}, \boldsymbol{b})] + (\boldsymbol{x} - \boldsymbol{x}_a)^T \mathbf{S}_a^{-1} (\boldsymbol{x} - \boldsymbol{x}_a), \quad (2)$$

where $\boldsymbol{y}$ is the HIRAS spectrum; $\mathbf{F}$ is the forward model of radiative transfer; $\boldsymbol{x}$ is the state vector consisting of to-be-retrieved variables; $\boldsymbol{b}$ is a set of input parameters that is not to be retrieved; $\mathbf{S}_\epsilon$ is the measurement error covariance matrix; $\mathbf{S}_a$ is the a priori covariance matrix for $\boldsymbol{x}$; $\boldsymbol{x}_a$ is

the a priori state vector. We assume that $\mathbf{S}_a$ is a diagonal matrix. In the spectral window from 1208.75 to 1400 cm-1, the main interfering gases include CH_4, N_2O, and H_2O. The spectral region from 1208.75 to 1300 cm^{-1}, which does not contain strong SO_2 absorption but has moderate H_2O absorption, is mainly used to better constrain H_2O and surface temperature.

Ideally for optimal estimation, all unknown variables should be included in the state vector. Instead, as in Carboni et al. (2012) and von Clarmann et al. (2001), they can be considered as unknowns that are not to be retrieved by the algorithm. Their contributions to the spectral variability can be included in the spectral error covariance matrix $\mathbf{S}_\varepsilon$. $\mathbf{S}_\varepsilon$ represents the spectral difference between calculated and observed spectra from the radiative transfer model simulations in the absence of SO_2, but with the best possible knowledge of all input parameters. Here, we use the observations of April 16, 2024, one day before the eruption, to construct $\mathbf{S}_\varepsilon$ under both clear and cloudy conditions. For each HIRAS spectrum, simulated spectra are generated using ERA5 reanalysis data as inputs with zero SO_2 amount. The resulting $\mathbf{S}_\varepsilon$ includes the spectral variability caused by errors in the observed spectra and the forward RT model, including the contribution from clouds unaccounted for in the RT model.

Since the SO_2 layer height has been retrieved in the previous step, the state vector in eq. (2) includes only the SO_2 total column and the surface skin temperature. In the algorithm, the a priori SO_2 layer (different from the a priori SO_2 background shown in **Fig. S2**) is assumed to be a 1-km thick layer with a 1-DU total column, centered at the height retrieved in the previous step. Note that the a priori SO_2 background is fixed and not adjusted during the retrieval process. The a priori error is set to 350 % for the SO_2 column and 20 K for the surface skin temperature. These large errors ensure that most of the retrieved SO_2 information comes from the measurements rather than the a priori. Based on the optimal estimation method, the inverse model in FY-LeoAIR uses the Levenberg-Marquardt modification of the Gauss-Newton method to minimize the cost function given by eq. (2). From the retrieval results, we obtain the a posteriori covariance matrix, from which the a posteriori error for the SO_2 column retrieval is derived. To screen the retrieval results, we use the reduced χ^2, which represents the quality of the spectral fit relative to the spectral error for each retrieval, as a post-filter (reduced $\chi^2 < 5.0$ and retrieved height > 5 km). Most retrievals yield a reduced χ^2 below 1.5, indicating a good spectral fit relative to the measurement error. In addition, we compare SO_2 columns retrieved from this study with those from the conventional optimal estimation method, which simultaneously retrieves all interfering gases (see Table 2) similar to **Zeng et al. (2023a)**. **Fig. S18** shows that the two methods produce consistent results.

3.5. Estimation of the e-folding time of volcanic SO_2 mass

To estimate the e-folding time of volcanic SO_2 mass due to removal processes of atmospheric SO_2 including chemical sinks that convert SO_2 to sulfate aerosols, the exponential decay equation is given by:

$$\boldsymbol{Mass}(\boldsymbol{t}) = \boldsymbol{Mass}(\boldsymbol{t0})^{*}\boldsymbol{e}^{-\frac{\boldsymbol{1}}{\boldsymbol{\tau}}}$$

where $Mass(t)$ is the volcanic SO_2 total mass at time t. τ is the e-folding time representing the rate of chemical conversion to sulfate aerosols.

4. Results

4.1. Retrievals of SO_2 columns and layer height from the HIRAS constellation

The Ruang volcano (2.3°N, 125.37°E) is located in Indonesia with a summit elevation of 725 m. According to **Global Volcanism Program (2024)**, on April 16, 2024, explosive activity began at 21:45 local time (LT) and ash plumes rose 2 km above the summit. At 01:08 LT on 17 April, an explosive pulse resulted in ash plumes rising to 9.1 km a.s.l. and drifting westwards. At 03:00 LT, the plumes reached 12.2 km a.s.l. and detached from the summit. This eruptive event is a good case study because of its intense eruptions and the long-range transport of the SO_2 plume (e.g., Dodangodage et al., 2025).

To detect the SO_2 plumes from the Ruang volcanic eruption, we calculate the HRI for all observations from April 17 to 29, 2024. Examples distributions are shown in Fig. 3. The signatures of the SO_2 plumes are evident with HRI values significantly higher than zero. The results show that the SO_2 plume propagates westwards and gradually dilutes as it travels. During the process, SO_2 chemically converts into sulfate aerosols. There are gaps between swaths of the satellite instruments which may lead to missing parts of the plume. Based on the HRI results, we extract plumes with an HRI value of 5 or higher, which corresponds to a high-confidence detection threshold. The retrieval algorithms for SO_2 column and layer height are then applied exclusively to these extracted plumes to reduce the computational burden.

Examples of SO_2 column retrievals are shown in Fig. 4**.** The corresponding spatial distribution of SO_2 layer height and histograms are shown in Figs. 5**, S3 and S4**. The full time series of SO_2 columns from April 17 to 29, 2024 is shown in **Movies S1**. The a posteriori error for SO_2 columns from the retrieval algorithm is about 6 % (**Fig. S5**). The results also show that the SO_2 columns and layer heights estimated from the three different HIRAS instruments are in good agreement. The largest SO_2 columns occurred on April 18, one day after the eruption.

Fig. 6(a) shows that the average SO_2 layer height detected by HIRAS starts at about 12.5 km, and slowly increases to a height of about 16 km, stabilizing from April 19, 3 days after the eruption. The plume height is expected to remain relatively constant as the plume stabilizes, so the standard deviation of 1.0 to 1.5 km (Fig. 6(a)) may represent the uncertainty in the SO_2 layer height estimate, which is consistent with the estimate made by Clarisse et al. (2014). The comparison of mean SO_2 layer height with IASI shows a good agreement starting from the 2nd day (April 18) after eruption, with a systematic difference (see next section for the quantitative comparison). IASI observed a lower height (~8 km) on the first day of eruption compared to HIRAS (~12 km). Both estimates on the first day show large uncertainties although their error bars overlap to some extent. This difference is probably due to a better spectral resolution of IASI, which allows it to detect deeper into the atmosphere, as the absorption lines are better resolved.

Note that FY-3D/HIRAS shows the largest variation although the mean values are close to the other HIRAS instruments. The tropopause is a barrier to the vertical transport of SO_2. To understand the location of the estimated plume height relative to the tropopause, we adopted the method in Clarisse et al. (2014) for deriving the thermal tropopause height in the study area (**Fig. S6**) using ERA5 reanalysis data. The tropopause is defined as the first vertical level which is above 4 km and has a lapse rate that is less than 0.1 K/km. Our estimate shows that the tropopause is larger than 17.5 km, which suggests that the SO_2 plume from the Ruang eruption remains largely below the tropopause.

To demonstrate the capabilities of HIRAS constellation in monitoring volcanic eruptions at high latitudes, we apply the method described above to the eruption of the Sheveluch volcano (56.653°N, 161.36°E; summit elevation of 3283 m) in Russia on November 2024. The results of HRI and SO_2 columns are shown in **Figs. S7–12**, respectively, for three representative days after the eruptions. According to **Global Volcanism Program (2024)**, a strong explosive eruption began at 19:19 (local time) on 7 November, that is UTC 7:19 on 7 November. Our results capture the elevated SO_2 plumes on the second day after the eruption. The evolution of the SO_2 plumes is evident in the spatial distributions of HRI and SO_2 column retrievals. In addition, the retrievals from the three HIRAS instruments are consistent. For high-latitude overpasses, overlapping observation regions among the three HIRAS sensors enable inter-comparisons at nearly coincident times. The HRI comparison results are shown in **Figs. S13 and S14**. During this period, three collocated overpasses can be found on November 11, 12, and 13. The time

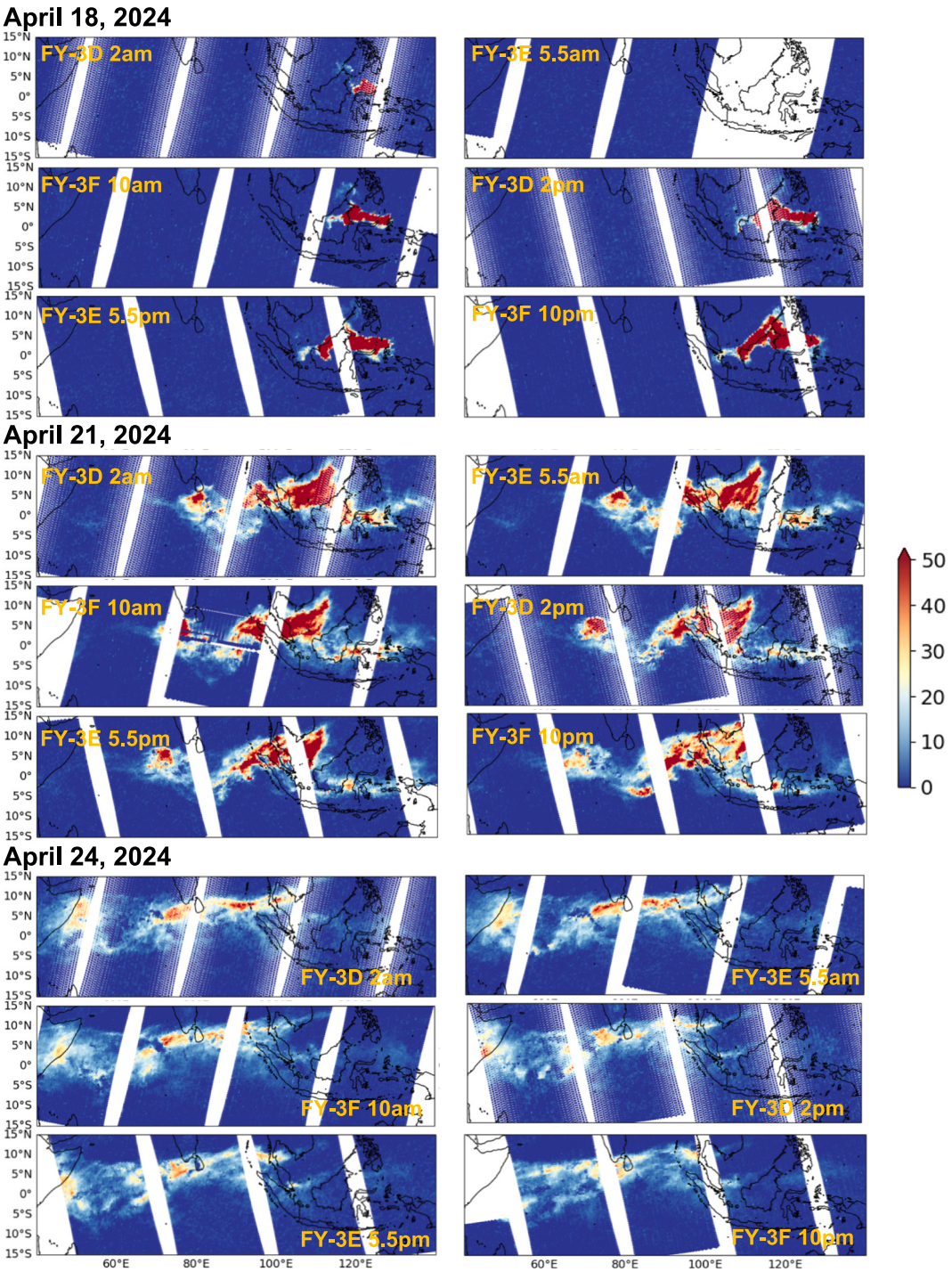

Fig. 3. Maps of SO_2 HRI for three representative days (April 18, 21, and 24) from FY-3D/HIRAS, FY-3E/HIRAS-II, and FY-3F/HIRAS-II.

difference between FY-3D and FY-3E overpasses is about 0.1 h, and less than 0.4 h between FY-3E and FY-3F overpasses. These collocated observations show correlation coefficients larger than 0.84 in all cases, suggesting high consistency among the HIRAS sensors in detecting the SO_2 signal. Our results further demonstrate the effectiveness of the HIRAS constellation to monitor volcanic SO_2 plumes from high-latitude volcanoes.

4.2. *Temporal evolution of SO_2 mass and estimation of SO_2 lifetime*

From the retrieved SO_2 columns, we can calculate the total SO_2 mass by integrating over the plume. Due to the footprint gaps between field-of-views, we re-grid the retrievals into regular grids (0.5° by 0.5°) with known areas before calculating the mass. On the other hand, for the gaps between HIRAS swaths, we used the observations from adjacent HIRAS swaths to fill the gaps. For example, the swath gaps in FY-3F/HIRAS are filled by the data in FY-3D, and vice versa, while the those in FY-3E/HIRAS are filled by FY-3F. Note that the HIRAS instruments on board FY-3D and FY-3E have overlapping swath gaps, making them suboptimal for filling each other's gaps. Since changes in SO_2 columns within the 4-h time difference are minimal, we expect the error caused by gap filling to be small. Examples of the SO_2 columns before and after gap-filling are shown in **Fig. S15**. To quantify the uncertainty due to the gap-filling procedure, in Fig. S16 we compare the SO2 columns from

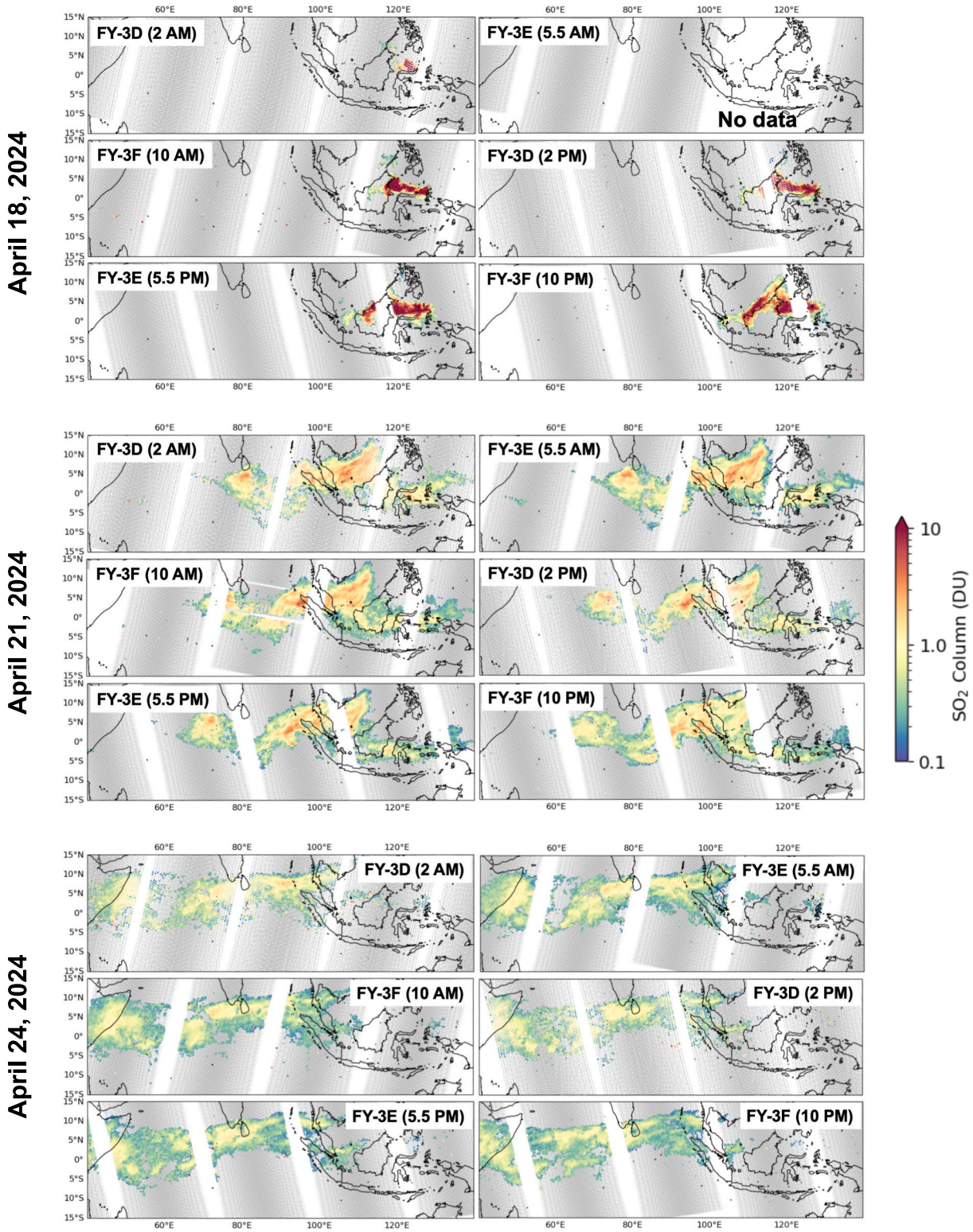

Fig. 4. The SO_2 total column estimates for three representative days from FY-3D/HIRAS, FY-3E/HIRAS-II, and FY-3F/HIRAS-II. The corresponding HRI maps are shown in Fig. 3.

different HIRAS sensors in overlapping observation regions. The average relative differences are 124 % between FY-3D and FY-3F, and 85 % between FY-3E and FY-3F. This discrepancy is mainly due to the movement of the SO_2 plumes over the 4-h interval between observations, which leads to spatial mismatches. Fortunately, the gap-filled SO_2 mass is only a small fraction of the total mass. On average, the gap-filled SO_2 mass accounts for 24 % for FY-3D, 17 % for FY-3E, and 12 % for FY-3F. Consequently, the estimated uncertainty in the total SO_2 mass due to gap-filling is 124 % × 24 % = 30 % for FY-3D, 85 % × 17 % = 14 % for FY-3E, and 124 % × 12 % = 15 % for FY-3F.

The SO_2 mass can be used to infer the volcanic flux and the SO_2 lifetime (Theys et al., 2013) in the atmosphere. Quantifying the

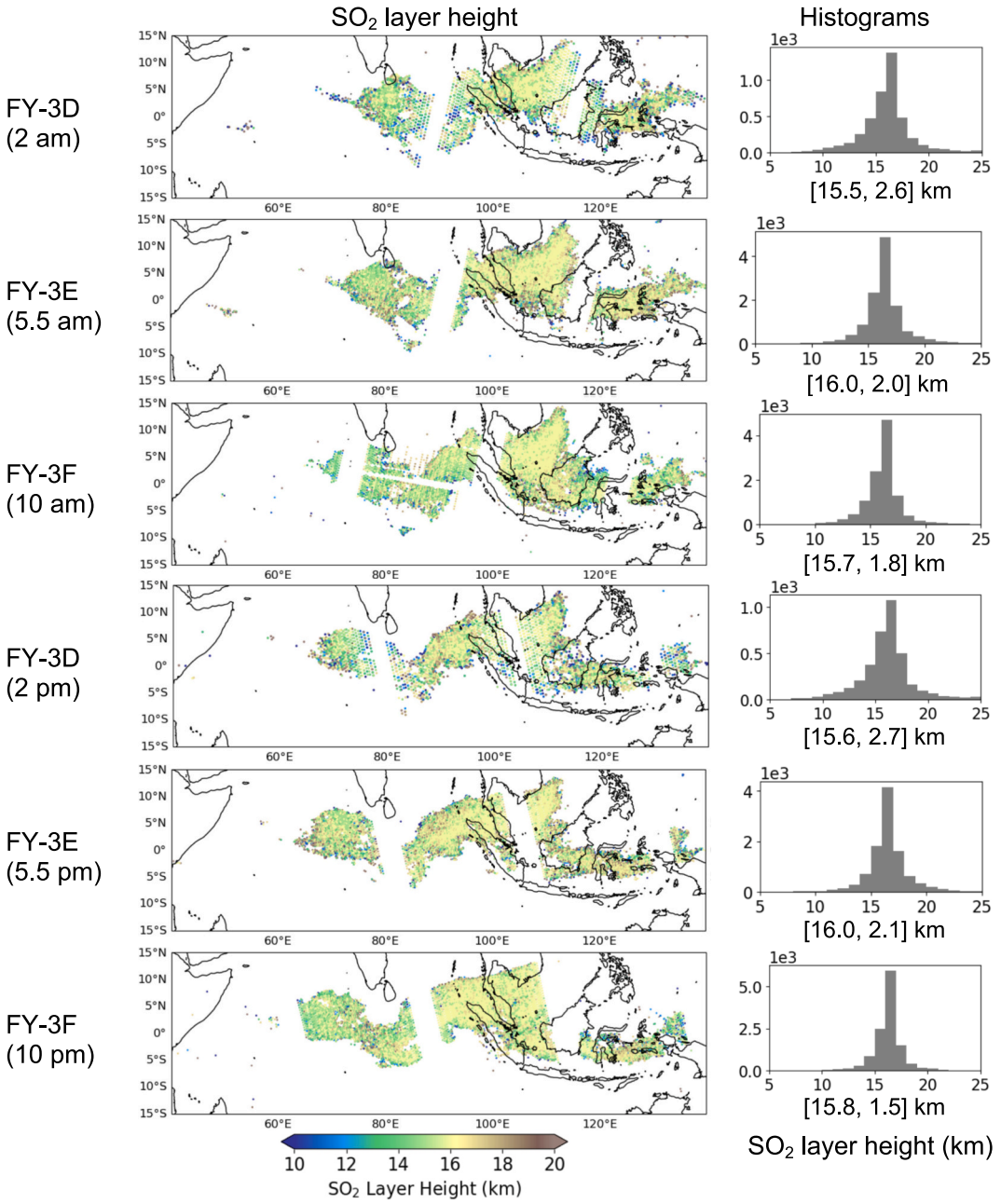

Fig. 5. The spatial distribution of the estimated SO_2 layer height and the corresponding histograms for the observations on April 21, 2024. The values of mean and standard deviation of the estimated SO_2 layer height are indicated below each histogram. The results on April 18 and April 24 are shown in Fig. S3 and Fig. S4, respectively.

atmospheric lifetime of SO_2 is important for flux inversion (Theys et al., 2013) and for assessing the potential impact of the eruptions on climate and local atmospheric chemistry. The time series of the estimated SO_2 mass from the HIRAS instruments are shown in Fig. 6(b). The largest SO_2 mass from HIRAS (around 200 ktons) occurred on April 19, 2024, the third day after the eruption. Thereafter, the SO_2 mass decreases steadily. Detection of the SO_2 plume becomes more difficult after April 29, 2024, so we stop tracking the plumes after this date. The total SO_2 mass on the last day is about 60 ktons. Note that the lower value of TROPOMI on the last day is caused by a smaller coverage of its detected plume (**Fig. S17**). The decrease in SO_2 mass fits very well with an exponential decay function (see Fig. 6(c)) with an e-folding time of 9.0 ± 2.8 days. Several sensitivity tests were carried out to assess the robustness of this estimate. When using observations from individual satellites, the estimated e-folding time and associated uncertainties are 10.4 ± 7.0 days for FY-3D, 7.4 ± 3.2 days for FY-3E, and 10.1 ± 5.9 days for FY-3F. These results suggest that from the use of the entire HIRAS constellation significantly reduces the uncertainty in the e-folding time estimate. The SO_2 decay derived in this study is representative of a plume in the UTLS (Carn et al., 2016). As mentioned by Theys et al. (2013), since satellite observations have a detection limit, parts of the diluted SO_2 plume that fall below this limit may go undetected. Consequently, the estimated e-folding lifetime is likely to be underestimated.

4.3. Cross-comparison with IASI and TROPOMI retrievals

As ground-based measurements are not available, we compare our results from HIRAS with data products from infrared IASI (version 4) and UV–Vis TROPOMI sensors. Both datasets have had wide applications (e.g., Taylor et al., 2018; Fioletov et al., 2020). The IASI SO2 retrieval

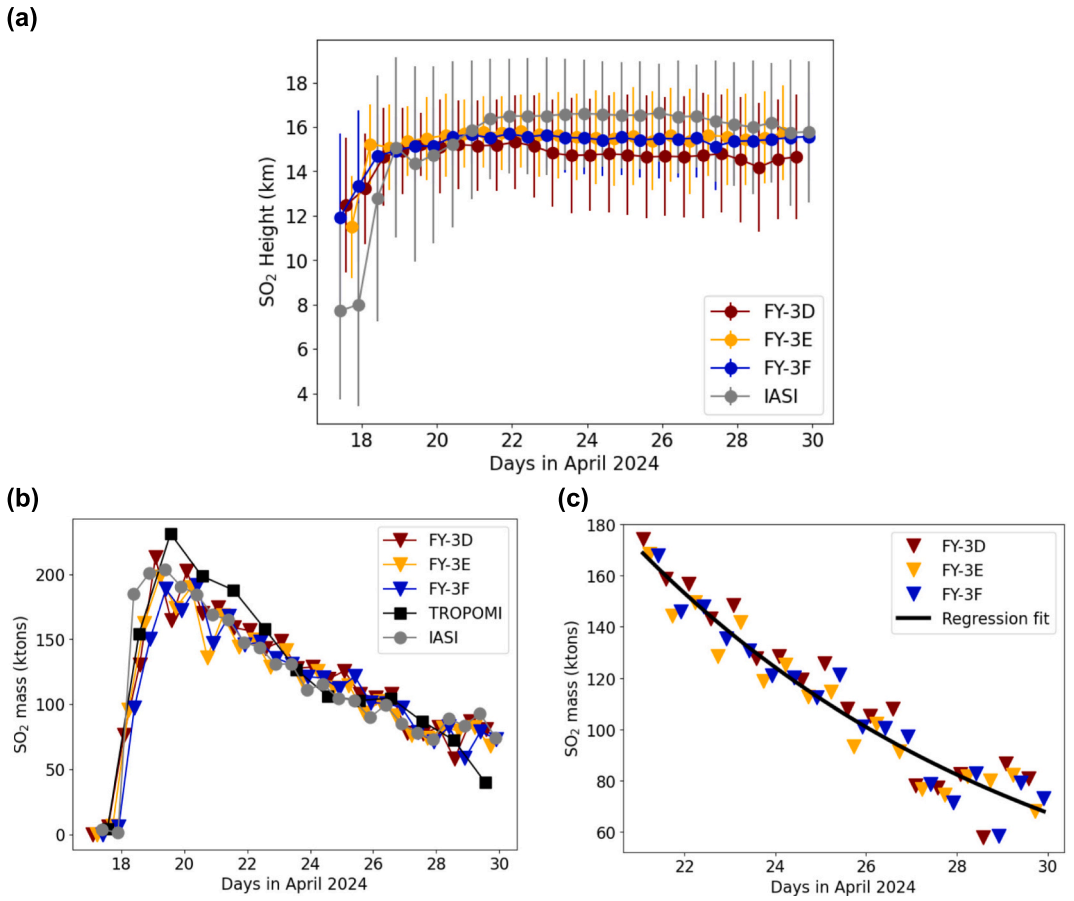

Fig. 6. (a) Time series of SO_2 layer height from the HIRAS instruments from April 17 to 29, 2024. The error bar represents the data variability; (b) Time series of SO_2 mass of the Ruang volcanic eruption from April 17 to 29, 2024 estimated from HIRAS. The swath gaps of the HIRAS data are filled based on the adjacent HIRAS observations, as explained in the text. The SO_2 masses from IASI/Metop-B and —C combined, and from TROPOMI are also shown. We have filtered out data with SO_2 less than 0.1 DU; (c) The regression fit using the exponential decay function (Text S2) from April 21, 2024. The e-folding time is estimated to be 9.0 days.

algorithm, based on Clarisse et al. (2014), shows similarities with the approach applied to HIRAS observations. For the TROPOMI SO_2 column, as described in Theys et al. (2021), the covariance-based retrieval algorithm retrieves only the SO_2 slant column density by using a measurement error covariance matrix similar to IASI and HIRAS.

For this comparison, we have re-gridded the data to the same 0.5° by 0.5° grids as HIRAS. Note that for TROPOMI, the SO_2 volume column densities (VCDs) were retrieved for an assumed fixed plume height of 15 km. Examples of the comparison results using morning observations on April 20, 2024 are shown in Fig. 7(a) for the total column between FY-3F/HIRAS-II and IASI, and Fig. 7(c) between FY-3D/HIRAS and TROPOMI, based on their proximity in equatorial crossing times. Highly consistent spatial observations can be observed. The comparison of all retrieved SO_2 columns from April 17 to 29, 2024 is shown in Fig. 7(b) and 7(d). The FY-3F/HIRAS-II and IASI have a correlation coefficient as high as 0.91. The root mean square error (RMSE) over this period is 0.53 DU. Similarly, the comparison of all SO_2 columns from FY-3D/HIRAS and TROPOMI shows a strong correlation of 0.86 and an RMSE of 0.6 DU. Relatively, the median difference is 26 % between FY-3F/HIRAS-II and IASI, and 44 % between FY-3D/HIRAS and TROPOMI.

For the SO_2 layer height, a comparison between FY-3F/HIRAS-II and IASI is shown (Fig. 7(e)). Unfortunately, no CALIPSO data is available for validation as the instrument ended its operation in mid-2023. The comparison results show that the SO_2 layer heights have a systematic difference of about 1.89 km, which is close to the uncertainty on the SO_2 layer height estimates. This difference may be caused by the settings in the forward radiative transfer model or the different spectral signal-to-noise ratios between HIRAS and IASI. Note that the correlation coefficient is low (0.17), which is expected since the SO_2 layer height changes only slightly after the plume ascends to the UTLS. The estimation uncertainty contributes to the spread of the data points, resulting in low correlation. Nevertheless, the HIRAS estimates successfully capture the general temporal evolution of the SO_2 layer height.

5. Discussion and conclusions

The low-Earth orbit constellation of HIRAS instruments on board China's FengYun-3 (FY-3) meteorological satellites fly in three different sun-synchronous orbits, including FY-3E (dawn-dusk orbit), FY-3F (mid-morning orbit), and FY-3D (afternoon orbit). This constellation provides six global coverages (roughly every 4-h) each day with equatorial overpass times at 5:30 am/pm, 10:00 am/pm, and 2:00 am/pm, respectively. Using the Ruang volcanic eruptions in mid-April 2024 as a case study, this study demonstrates the capability of the HIRAS constellation to track volcanic SO_2 plumes at a high observation frequency of every four hours. Our results show that the HIRAS constellation captures well the spatial and vertical variability of the lofted volcanic SO_2 plume, in good agreement with existing data products from IASI and TROPOMI satellites. In addition, the time series of the SO_2 mass is used to estimate the e-folding decay time of the mass (9.0 ± 2.8 days). Furthermore, we apply the methods to the eruptions of the Russia's Sheveluch volcano in November 2024 at high latitudes. The evolution of the volcanic SO_2 can be effectively monitored by the HIRAS constellation and the consistency among the HIRAS sensors in detecting the SO_2 signal is demonstrated. This study is an important milestone towards a global constellation of hyperspectral infrared sounders to monitor global

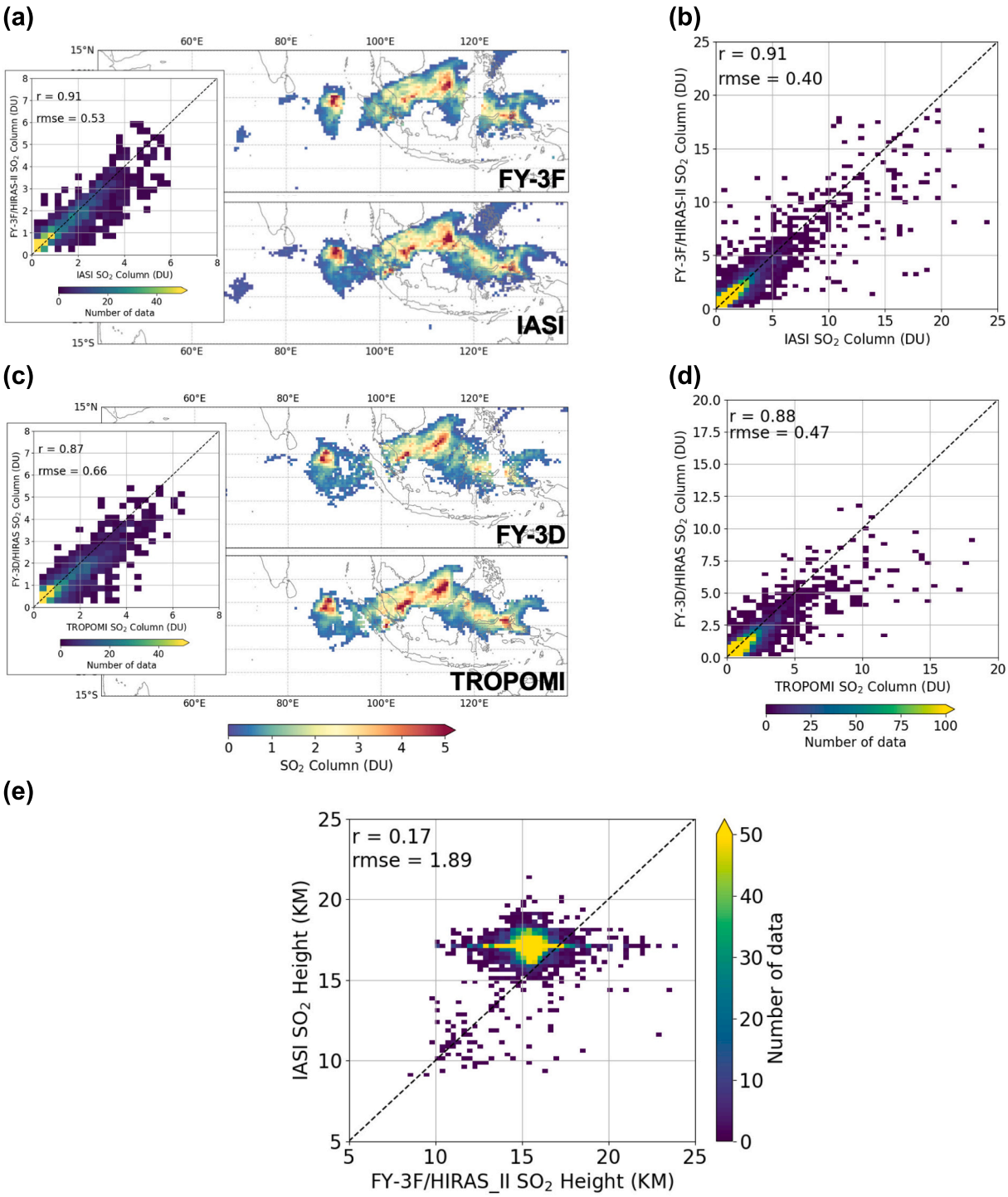

Fig. 7. (a) Example of SO_2 column comparison between IASI and FY-3F/HIRAS-II on April 20, 2024 in the daytime (~10 am). For IASI, only the SO_2 column data greater than 0.25 DU are used. Data from IASI onboard Metop-B and —C are combined before gridding. The SO_2 column data are averaged over 0.5° by 0.5° grids before making the comparison; (b) Same as (a) but for all days from April 17 to 29, 2024. About 14 points larger than 25 DU are not shown. The total number of data is about 27,000; (c) similar to (a) but for examples between FY-3D/HIRAS-II and TROPOMI in the daytime (~1:30 pm). Only the TROPOMI data greater than 0.25 DU are used; (d) Same as (c) but for all days from April 17 to 29, 2024. About 7 points greater than 20 DU are not shown. The total number of data is about 11,000; (e) A comparison of SO_2 layer height between IASI and FY-3F/HIRAS-II from April 17 to 29, 2024. The data have been averaged over 1° by 1° grids before the comparison.

variations of atmospheric composition.

The frequent overpasses by the HIRAS constellation (occurring at least every 4 h) offer significant potential for applications in climate modelling, air quality monitoring, and volcanology. These opportunities warrant thorough exploration in future studies. The potential applications include: (1) Hazard mitigation. The constellation with high revisit frequency makes it possible to catch large eruptions in their early stages. With a single instrument, in the worst case, an eruption may be missed by a short period of time and only detected 12 h later (or 24 h in case of UV/Vis sounders). This is particularly important for remote and unmonitored volcanoes; (2) Inverse modelling and assimilation to improve knowledge of volcanic SO_2 fluxes. Models can be used to obtain accurate estimates of SO_2 fluxes and injection heights by assimilating satellite data. These injection heights can be used to obtain improved SO_2

retrievals from satellites, which in turn improves the estimation of SO_2 fluxes (e.g., Pardini et al., 2019). A constellation with frequent overpasses will certainly facilitate this. In addition, SO_2 fluxes can also be estimated without the use of complex models (e.g., Theys et al., 2013). More frequent overpasses should lead to improved estimates and allow the derivation of the atmospheric lifetime of SO_2.

To further increase the observation frequency would require a global constellation of geostationary infrared sounders (e.g., Li et al., 2022; He et al., 2025) with SO_2 detection capabilities. Currently, these include the existing and upcoming GIIRS instruments on board China's FY-4 series over East Asia and the recently launched (in July 2025) infrared sounder - Meteosat Third Generation (IRS/MTG) over Europe. These geostationary sensors would provide revisit times of 2 h for GIIRS and 30 or 60 min for IRS. However, current GIIRS and IRS instruments do not encompass the $\nu 3$ absorption band but only the less intense $\nu 1$ band of SO_2. Consequently, although the geostationary sounders have the advantage of higher frequency observations, the current polar-orbiting sounders (e.g., CrIS, HIRAS, and IASI) will remain better for robust and more accurate retrieval of volcanic SO_2. In addition, in regions not covered by geostationary sensors, such as much of the Southern Hemisphere, the HIRAS constellation described in this study would provide critical datasets for monitoring volcanic SO_2.

CRediT authorship contribution statement

Zhao-Cheng Zeng: Writing – review & editing, Writing – original draft, Visualization, Validation, Software, Resources, Project administration, Methodology, Investigation, Funding acquisition, Formal analysis, Data curation, Conceptualization. **Lieven Clarisse:** Writing – review & editing, Validation, Resources, Data curation. **Bruno Franco:** Writing – review & editing, Validation, Resources, Data curation. **Cathy Clerbaux:** Writing – review & editing, Validation, Resources, Data curation. **Nicolas Theys:** Writing – review & editing, Validation, Resources, Data curation. **Chengli Qi:** Writing – review & editing, Resources, Data curation. **Lu Lee:** Writing – review & editing, Resources, Data curation. **Lin Zhu:** Writing – review & editing, Data curation. **Xiuqing Hu:** Writing – review & editing, Resources, Data curation. **Mingjian Gu:** Writing – review & editing, Resources, Data curation. **Peng Zhang:** Writing – review & editing, Resources, Data curation.

Declaration of competing interest

The authors declare that they have no known competing financial interests or personal relationships that could have appeared to influence the work reported in this paper.

Acknowledgements

Z.-C. Zeng acknowledges funding from the National Natural Science Foundation of China (Grant 12292980 and 42275142) and the National Key R&D Program of China (Grant 2022YFA1003800). This work was also supported by High Performance Computing Platform of Peking University. N. Theys acknowledges financial support from ESA S5P PAL, ESA S5P ATM-MPC and Belgium Prodex TRACE-S5P projects. L. Clarisse is a Senior Research Associate with the Fonds de la Recherche Scientifique – FNRS. Cathy Clerbaux is grateful to CNES for financial support. The research at ULB has been supported by the IASI.Flow Prodex arrangement (ESA–BELSPO).

Appendix A. Supplementary data

Supplementary data to this article can be found online at https://doi.org/10.1016/j.rse.2025.115057.

Data availability

The SO_2 retrieval data from HIRAS in this study are available at https://doi.org/10.5281/zenodo.17239336. Further updates on the HIRAS SO_2 data will be posted on the FengYun-AIR project website: https://fengyunair.github.io/. FY-3/HIRAS Level 1 data are publicly available from the FengYun Satellite Data Center (https://data.nsmc.org.cn/DataPortal/en/home/index.html); The IASI SO2 retrieval data presented in this paper are publicly available from the IASI Portal (https://iasi.aeris-data.fr/). TROPOMI SO_2 data are available on the S5P-PAL Data Portal (https://data-portal.s5p-pal.com/products/so2cbr.html).

References

Atmospheric and Environmental Research, 2025. Line-by-line radiative transfer model (LBLRTM). Atmos. Environ. Res. Retrieved from https://github.com/AER-RC/LBLRTM.

Carboni, E., Grainger, R., Walker, J., Dudhia, A., Siddans, R., 2012. A new scheme for sulphur dioxide retrieval from IASI measurements: application to the Eyjafjallajökull eruption of April and May 2010. Atmos. Chem. Phys. 12, 11417–11434. https://doi.org/10.5194/acp-12-11417-2012.

Carn, S.A., Strow, L.D., de Souza-Machado, S., Edmonds, Y., Hannon, S., 2005. Quantifying tropospheric volcanic emissions with AIRS: the 2002 eruption of Mt. Etna (Italy). Geophys. Res. Lett. 32 (2). https://doi.org/10.1029/2004GL021034.

Carn, S.A., Krueger, A.J., Arellano, S., Krotkov, N.A., Yang, K., 2008. Daily monitoring of Ecuadorian volcanic degassing from space. J. Volcanol. Geotherm. Res. 176 (1), 141–150. https://doi.org/10.1016/j.jvolgeores.2008.01.029.

Carn, S.A., Clarisse, L., Prata, A.J., 2016. Multi-decadal satellite measurements of global volcanic degassing. J. Volcanol. Geotherm. Res. 311, 99–134. https://doi.org/10.1016/j.jvolgeores.2016.01.002.

Clarisse, L., Coheur, P.F., Prata, A.J., Hurtmans, D., Razavi, A., Phulpin, T., et al., 2008. Tracking and quantifying volcanic SO2 with IASI, the September 2007 eruption at Jebel at Tair. Atmos. Chem. Phys. 8, 7723–7734. https://doi.org/10.5194/acp-8-7723-2008.

Clarisse, L., Coheur, P.-F., Theys, N., Hurtmans, D., Clerbaux, C., 2014. The 2011 Nabro eruption, a SO2 plume height analysis using IASI measurements. Atmos. Chem. Phys. 14, 3095–3111. https://doi.org/10.5194/acp-14-3095-2014.

Clerbaux, C., Coheur, P.-F., Clarisse, L., Hadji-Lazaro, J., Hurtmans, D., Turquety, S., et al., 2008. Measurements of SO2 profiles in volcanic plumes from the NASA tropospheric emission spectrometer (TES). Geophys. Res. Lett. 35, L22807. https://doi.org/10.1029/2008GL035566.

Dodangodage, R., Bernath, P.F., Wyatt, M., Boone, C., 2025. Atmospheric chemistry experiment (ACE) satellite observations of aerosols and SO2 emissions from the 2024 Ruang volcanic eruption. J. Quant. Spectrosc. Radiat. Transf. https://doi.org/10.1016/j.jqsrt.2024.109333.

Fioletov, V., McLinden, C.A., Griffin, D., Theys, N., Loyola, D.G., Hedelt, et al., 2020. Anthropogenic and volcanic point source SO2 emissions derived from TROPOMI on board Sentinel-5 Precursor: first results. Atmos. Chem. Phys. 20, 5591–5607. https://doi.org/10.5194/acp-20-5591-2020.

Global Volcanism Program, 2024. Report on Ruang (Indonesia). In: Sennert, S. (Ed.), Weekly Volcanic Activity Report, 17 April-23 April 2024. Smithsonian Institution and US Geological Survey.

Halmer, M., Schmincke, H.-U., Graf, H.-F., 2002. The annual volcanic gas input into the atmoshpere, in particular into the stratosphere: a global data set for the past 100 years. J. Volcanol. Geotherm. Res. 115, 511–528. https://doi.org/10.1016/S0377-0273(01)00318-3.

He, T.L., Oomen, G.M., Tang, W., Bouarar, I., Chance, K., Clerbaux, C., et al., 2025. Challenges and opportunities offered by geostationary space observations for air quality research and emission monitoring. Bull. Am. Meteorol. Soc. 106 (5), E939–E963. https://doi.org/10.1175/BAMS-D-23-0145.1.

Hersbach, H., Bell, B., Berrisford, P., Hirahara, S., Horanyi, A., Munoz-Sabater, J., et al., 2020. The ERA5 global reanalysis. Q. J. R. Meteorol. Soc. 146, 1999–2049. https://doi.org/10.1002/qj.3803.

Hua, J., Liu, S., Qi, C., Wu, S., Lee, L., Hu, X., et al., 2025. Observing carbon monoxide and volatile organic compounds from Canadian wildfires in 2023 from FengYun-3E/HIRAS-II in a dawn-dusk sun-synchronous orbit. Remote Sens. Environ. 327, 114829. https://doi.org/10.1016/j.rse.2025.114829.

Hyman, D.M., Pavolonis, M.J., 2020. Probabilistic retrieval of volcanic SO2 layer height and partial column density using the Cross-track Infrared Sounder (CrIS). Atmos. Meas. Tech. 13, 5891–5921. https://doi.org/10.5194/amt-13-5891-2020.

Inness, A., Ades, M., Agustí-Panareda, A., Barré, J., Benedictow, A., Blechschmidt, et al., 2019. The CAMS reanalysis of atmospheric composition. Atmos. Chem. Phys. 19, 3515–3556. https://doi.org/10.5194/acp-19-3515-2019.

Krueger, A., Walter, L.S., Bhartia, P.K., Schnetzler, C.C., Krotkov, N.A., Sprod, I., et al., 1995. Volcanic sulfur-dioxide measurements from the total ozone mapping spectrometer instruments. J. Geophys. Res. 100, 14,057–14,076.

Lee, C., Richter, A., Weber, M., Burrows, J.P., 2008. SO_2 retrieval from SCIAMACHY using the weighting function DOAS (WFDOAS) technique: comparison with standard DOAS retrieval. Atmos. Chem. Phys. 8, 6,137–6,145. https://doi.org/10.5194/acp-8-6137-2008.

Li, J., Menzel, W.P., Schmit, T.J., Schmetz, J., 2022. Applications of geostationary hyperspectral infrared sounder observations: progress, challenges, and future perspectives. Bull. Am. Meteorol. Soc. 103, E2733–E2755. https://doi.org/10.1175/BAMS-D-21- 0328.1.

Li, X., Zhu, L., Sun, H., Li, J., Lv, X., Qi, C., Yan, H., 2025. A channel selection methodology for enhancing volcanic SO_2 monitoring using FY-3E/HIRAS-II hyperspectral data. Atmos. Meas. Tech. 18, 2333–2352. https://doi.org/10.5194/amt-18-2333-2025.

Liang, Z., Gu, D., Li, R., Liu, J., Zhai, C., Su, H., Lau, A.K., 2025. Advancing atmospheric detection of weakly absorbing reactive trace gases using the FY-3E/HIRAS-II TIR sounder on a dawn–dusk orbit. Environ. Sci. Technol. Lett. 12 (7). https://doi.org/10.1021/acs.estlett.5c00501.

Masuda, K., Takashima, T., Takayama, Y., 1998. Emissivity of pure and sea waters for the model sea surface in the infrared window regions. Remote Sens. Environ. 24, 313–329. https://doi.org/10.1016/0034-4257(88)90032-6.

Pardini, F., Queißer, M., Naismith, A., Watson, I.M., Clarisse, L., Burton, M.R., 2019. Initial constraints on triggering mechanisms of the eruption of Fuego volcano (Guatemala) from 3 June 2018 using IASI satellite data. J. Volcanol. Geotherm. Res. 376, 54–61. https://doi.org/10.1016/j.jvolgeores.2019.03.014.

Prata, A.J., 1989. Observations of volcanic ash clouds in the 10–12 mm window using AVHRR/2 data. Int. J. Remote Sens. 10, 751–761.

Prata, A.J., 2009. Satellite detection of hazardous volcanic clouds and the risk to global air traffic. Nat. Hazards 51, 303–324. https://doi.org/10.1007/s11069-008-9273-z.

Prata, A.J., Kerkmann, J., 2007. Simultaneous retrieval of volcanic ash and SO2 using MSG-SEVIRI measurements. Geophys. Res. Lett. 34 (5).

Prata, A.J., Rose, W.I., Self, S., O'Brien, D.M., 2003. Global, long-term Sulphur dioxide measurements from TOVS data: A new tool for studying explosive volcanism and climate. In: Robock, A., Oppenheimer, C. (Eds.), Volcanism and the Earth's Atmosphere, Geophys. Monogr. Ser., Vol. 139. AGU, Washington, D. C, pp. 1293–1296.

Pugnaghi, S., Gangale, G., Corradini, S., Buongiorno, M.F., 2006. Mt. Etna sulfur dioxide flux monitoring using ASTER-TIR data and atmospheric observations. J. Volcanol. Geotherm. Res. 152, 74–90.

Pumphrey, H.C., Read, W.G., Livesey, N.J., Yang, K., 2015. Observations of volcanic SO2 from MLS on Aura. Atmos. Meas. Tech. 8, 195–209. https://doi.org/10.5194/amt-8-195-2015.

Qi, C., Wu, C., Hu, X., Xu, H., Lee, L., Zhou, F., et al., 2020. High Spectral Infrared Atmospheric Sounder (HIRAS): System Overview and On-Orbit Performance Assessment. IEEE Trans. Geosci. Remote Sens. 58 (6), 4335–4352. https://doi.org/10.1109/TGRS.2019.2963085.

Queißer, M., Burton, M., Theys, N., et al., 2019. TROPOMI enables high resolution SO_2 flux observations from Mt. Etna, Italy, and beyond. Sci. Report. 9, 957. https://doi.org/10.1038/s41598-018-37807-w.

Rix, M., Valks, P., Hao, N., Loyola, D., Schlager, H., Huntrieser, H., et al., 2012. Volcanic SO2, BrO and plume height estimations using GOME-2 satellite measurements during the eruption of Eyjafjallajökull in May 2010. J. Geophys. Res. 117. https://doi.org/10.1029/2011JD016718. D00U19.

Robock, A., 2000. Volcanic eruptions and climate. Rev. Geophys. 38 (2), 191–219.

Rodgers, C.D., 2000. Inverse Methods for Atmospheric Sounding: Theory and Practice. World Scientific, River Edge, N.J., USA.

Seemann, S.W., Borbas, E.E., Knuteson, R.O., Stephenson, G.R., Huang, H.-L., 2008. Development of a global infrared land surface emissivity database for application to clear sky sounding retrievals from multispectral satellite radiance measurements. J. Appl. Meteorol. Climatol. 47, 108–123. https://doi.org/10.1175/2007JAMC1590.1.

Sellitto, P., Siddans, R., Belhadji, R., Carboni, E., Legras, B., Podglajen, A., et al., 2024. Observing the SO2 and sulfate aerosol plumes from the 2022 Hunga eruption with the infrared atmospheric sounding interferometer (IASI). Geophys. Res. Lett. 51. https://doi.org/10.1029/2023GL105565 e2023GL105565.

Taylor, I.A., Preston, J., Carboni, E., Mather, T.A., Grainger, R.G., Theys, N., et al., 2018. Exploring the utility of IASI for monitoring volcanic SO2 emissions. J. Geophys. Res. Atmos. 123, 5588–5606. https://doi.org/10.1002/2017JD027109.

Theys, N., Campion, R., Clarisse, L., Brenot, H., van Gent, J., Dils, B., et al., 2013. Volcanic SO2 fluxes derived from satellite data: a survey using OMI, GOME-2, IASI and MODIS. Atmos. Chem. Phys. 13, 5945–5968. https://doi.org/10.5194/acp-13-5945-2013.

Theys, N., Fioletov, V., Li, C., De Smedt, I., Lerot, C., McLinden, C., et al., 2021. A sulfur dioxide covariance-based retrieval algorithm (COBRA): application to TROPOMI reveals new emission sources. Atmos. Chem. Phys. 21, 16727–16744.

von Clarmann, T., Grabowski, U., Kiefer, M., 2001. On the role of non-random errors in inverse problems in radiative transfer and other applications. J. Quant. Spectrosc. Radiat. Transf. 71, 39–46.

Walker, J.C., Dudhia, A., Carboni, E., 2011. An effective method for the detection of trace species demonstrated using the MetOp infrared atmospheric sounding interferometer. Atmos. Meas. Tech. 4, 1567–1580. https://doi.org/10.5194/amt-4-1567-2011.

Watson, I.M., Realmuto, V.J., Rose, W.I., Prata, A.J., Bluth, G.J., et al., 2004. Thermal infrared remote sensing of volcanic emissions using the moderate resolution imaging spectroradiometer. J. Volcanol. Geotherm. Res. 135, 75–89.

Wu, C., Qi, C., Hu, X., Gu, M., Yang, T., Xu, H., et al., 2020. FY-3D HIRAS radiometric calibration and accuracy assessment. IEEE Trans. Geosci. Remote Sens. 58 (6), 3965–3976. https://doi.org/10.1109/TGRS.2019.2959830.

Xie, M., Gu, M., Zhang, C., Hu, Y., Yang, T., Huang, P., Li, H., 2023. Comparative study of the atmospheric gas composition detection capabilities of FY-3D/HIRAS-I and FY-3E/HIRAS-II based on information capacity. Remote Sens 15 (16), 4096. https://doi.org/10.3390/rs15164096.

Zeng, Z.-C., 2025. Global carbon monoxide retrieval from the hyperspectral infrared atmospheric sounder-II onboard FengYun-3E in a dawn-dusk sun- synchronous orbit. J. Quant. Spectrosc. Radiat. Transf. https://doi.org/10.1016/j.jqsrt.2024.109336.

Zeng, Z.-C., Lee, L., Qi, C., 2023a. Diurnal carbon monoxide observed from a geostationary infrared hyperspectral sounder: first result from GIIRS on board FengYun-4B. Atmos. Meas. Tech. 16, 3059–3083. https://doi.org/10.5194/amt-16-3059-2023.

Zeng, Z.-C., Lee, L., Qi, C., Clarisse, L., Van Damme, M., 2023b. Optimal estimation retrieval of tropospheric ammonia from the geostationary interferometric infrared sounder on board FengYun-4B. Atmos. Meas. Tech. 16, 3693–3713. https://doi.org/10.5194/amt-16-3693-2023.

Zeng, Z.-C., Franco, B., Clarisse, L., Lee, L., Qi, C., Lu, F., 2024. Observing a volatile organic compound from a geostationary infrared sounder: HCOOH from FengYun-4B/ GIIRS. J. Geophys. Res. Atmos. 129. https://doi.org/10.1029/2024JD041352 e2024JD041352.

Zhang, P., Hu, X.Q., Lu, Q.F., Zhu, A.J., Lin, M.Y., Sun, L., et al., 2022a. FY-3E: the first operational meteorological satellite mission in an early morning orbit. Adv. Atmos. Sci. 39, 1–8.

Zhang, C., Qi, C., Yang, T., Gu, M., Zhang, P., Lee, L., et al., 2022b. Evaluation of FY-3E/HIRAS-II radiometric calibration accuracy based on OMB analysis. Remote Sens 14 (13), 3222. https://doi.org/10.3390/rs14133222.

Zhang, P., Hu, X., Sun, L., Xu, N., Chen, L., Zhu, A., et al., 2024. The on-orbit performance of FY-3E in an early morning orbit. Bull. Am. Meteorol. Soc. 105 (1), E144–E175. https://doi.org/10.1175/BAMS-D-22-0045.1.

Zhou, M., Deng, Z., Robert, C., Zhang, X., Zhang, L., Wang, Y., Qi, C., Wang, P., Mazière, M.D., 2024. The first global map of atmospheric ammonia (NH_3) as observed by the HIRAS/FY-3D satellite. Adv. Atmos. Sci. 41 (3), 379–390. https://doi.org/10.1007/s00376-023-3059-9.